



This open access document is posted as a preprint in the Beilstein Archives at <https://doi.org/10.3762/bxiv.2021.30.v1> and is considered to be an early communication for feedback before peer review. Before citing this document, please check if a final, peer-reviewed version has been published.

This document is not formatted, has not undergone copyediting or typesetting, and may contain errors, unsubstantiated scientific claims or preliminary data.

**Preprint Title** Local stiffness and work-function variations of hexagonal boron nitride on Cu(111)

**Authors** Abhishek Grewal, Yuqi Wang, Matthias Münks, Klaus Kern and Markus Ternes

**Publication Date** 31 März 2021

**Article Type** Letter

**ORCID® IDs** Abhishek Grewal - <https://orcid.org/0000-0002-4566-8499>; Markus Ternes - <https://orcid.org/0000-0001-6800-4129>

License and Terms: This document is copyright 2021 the Author(s); licensee Beilstein-Institut.

This is an open access work under the terms of the Creative Commons Attribution License (<https://creativecommons.org/licenses/by/4.0>). Please note that the reuse, redistribution and reproduction in particular requires that the author(s) and source are credited and that individual graphics may be subject to special legal provisions.

The license is subject to the Beilstein Archives terms and conditions: <https://www.beilstein-archives.org/xiv/terms>.

The definitive version of this work can be found at <https://doi.org/10.3762/bxiv.2021.30.v1>

# 1 **Local stiffness and work-function variations of hexagonal boron ni-** 2 **tride on Cu(111)**

3 Abhishek Grewal<sup>\*1</sup>, Yuqi Wang<sup>1,2</sup>, Matthias Munks<sup>1</sup>, Klaus Kern<sup>1,3</sup> and Markus Ternes<sup>\*1,2,4</sup>

4 Address: <sup>1</sup>Max Planck Institut für Festkörperforschung, Heisenbergstrasse 1, D-70569 Stuttgart,

5 Germany; <sup>2</sup>Peter Grünberg Institute, Forschungszentrum Jülich, D-52425 Jülich, Germany;

6 <sup>3</sup>Institut de Physique, École Polytechnique Fédérale de Lausanne, CH-1015 Lausanne, Switzerland

7 and <sup>4</sup>II. Institute of Physics, RWTH Aachen University, D-52074 Aachen, Germany

8 Email: Abhishek Grewal - a.grewal@fkf.mpg.de; Markus Ternes - ternes@physik.rwth-aachen.de

9 \* Corresponding author

## 10 **Abstract**

11 Combined scanning tunnelling and atomic force microscopy using a qPlus sensor enables the  
12 measurement of electronic and mechanic properties of two dimensional (2D) materials at the  
13 nanoscale. In this work we study hexagonal boron nitride (*h*-BN), an atomically thin 2D layer,  
14 that is van der Waals coupled to a Cu(111) surface. The system is of interest as a decoupling layer  
15 for functional 2D heterostructures due to the preservation of the *h*-BN bandgap and as a template  
16 for atomic and molecular adsorbates owing to its local electronic trapping potential due to in-  
17 plane electric field. We obtain work-function ( $\Phi$ ) variations on the *h*-BN/Cu(111) superstructure  
18 in the order of 100 meV using two independent methods, namely the shift of field emission reso-  
19 nances (FER) and contact potential difference (CPD) measured by Kelvin probe force microscopy  
20 (KPFM). Using 3D force profiles of the same area we determine the relative stiffness of the Moiré  
21 region allowing us to analyse both electronic and mechanical properties of the 2D layer simultane-  
22 ously. We obtain a sheet stiffness of  $9.4 \pm 0.9 \text{ N m}^{-1}$  which is an order of magnitude higher than the  
23 one obtained for *h*-BN/Rh(111). Using constant force maps we are able to derive height profiles of

24 the *h*-BN/Cu(111) showing that the system has a corrugation of  $0.6 \pm 0.2 \text{ \AA}$  which helps demystify  
25 discussion around the flatness of the *h*-BN/Cu(111) substrate.

## 26 **Keywords**

27 hexagonal boron nitride; decoupling layers; Moiré superstructure; work-function variation; local  
28 stiffness

## 29 **Introduction**

30 Two-dimensional hexagonal boron nitride (*h*-BN) is among the list of materials that garnered  
31 tremendous interest following the exfoliation of mono- and few-layer thick graphene films [1,2].  
32 Unique properties like high thermal stability and conductivity, immense intra-sheet stiffness, and  
33 excellent dielectric properties make *h*-BN interesting for technological applications. For example,  
34 thin films of *h*-BN have been used as a passivating layer for graphene and MoS<sub>2</sub>-based electro-  
35 nics utilising the small lattice mismatch, the large optical phonon modes, and particularly the large  
36 bandgap [3-10]. Furthermore, when grown on metal substrates *h*-BN can be used as a nanotem-  
37 plate for atoms, molecules, and nanostructures with well controlled adsorption and electronic prop-  
38 erties [11-18]. In such systems, *h*-BN shows a rich structural and electronic morphology which  
39 depends on the lattice mismatch and the interaction strength with the substrate: Large and flat  
40 lattice-matched terraces for *h*-BN/Ni(111) [19,20], strain-induced highly-corrugated layers for *h*-  
41 BN/Rh(111) [21-23], and template layers for molecules with strong local variations of the work-  
42 function for *h*-BN/Ir(111) [24] are representative of such morphological diversity.

43 We use low-temperature combined scanning tunnelling (STM) and non-contact atomic force mi-  
44 croscopy (nc-AFM) to study *h*-BN on Cu(111). This template has interesting properties because  
45 the dielectric layer is only very weakly bound to the metal and shows an electronically induced  
46 Moiré superstructure [25,26]. First STM studies on this system pointed to only a small geometrical  
47 corrugation [27]. Further experimental investigations, using both local probes and averaging tech-  
48 niques, revealed more details of the mechanical and electronic properties of the system, but also  
49 inconsistent results about the structural corrugation [26,28-30]. For example, Brülke *et al.* used

50 high-resolution low energy electron diffraction and normal incidence X-ray standing wave tech-  
51 niques to detect the large separation of  $3.24 \text{ \AA}$  between the *h*-BN sheet and the topmost Cu(111)  
52 layer [29]. They found almost no height difference between B and N atoms and excluded signifi-  
53 cant buckling perpendicular to the surface. Interestingly, this stays in contrast to measurements by  
54 Schwarz *et al.* which used a more local analysis of the corrugation by exploiting nc-AFM conclud-  
55 ing an absolute height difference of  $0.3 - 0.7 \text{ \AA}$  between "rim" and "valley" sites of the spatially  
56 corrugated monolayer [26]. Recently, however, Zhang *et al.* used STM in combination with DFT  
57 simulations to study the variation of the local work-function and bandgap within the Moiré super-  
58 lattice and found that the variation depends on the angle of the Moiré with respect to the substrate  
59 lattice, but inferred only marginal structure modulation [30].

60 To shed more light on this controversy we use an alternative method to verify the mechanical prop-  
61 erties of the monolayer by measuring the stiffness of the *h*-BN layer at different locations of the  
62 superstructure and comparing these results with concomitantly recorded local work-function vari-  
63 ations. We determine the stiffness of the system by mapping and comparing the short-range inter-  
64 action forces between the monolayer and the probing metallic tip [31]. This technique enables us to  
65 detect the sheet stiffness with unprecedented spatial resolution [23]. On *h*-BN/Rh(111), a different  
66 system than studied in this work, the extremely low stiffness of only  $\approx 1 \text{ N m}^{-1}$  at the weakly bound  
67 rim areas confirmed the buckling of the monolayer into the third-dimension to relieve the strain  
68 induced by the significant lattice mismatch of this strongly corrugated van der Waals layer [23].

## 69 **Results and Discussion**

### 70 **STM/AFM on *h*-BN/Cu(111)**

71 As illustrated in Figure 1(a), we employ nc-AFM to probe the electronic and topographic structure  
72 of a monolayer of *h*-BN on the Cu(111) surface. Figure 1(b) shows a typical large scale constant-  
73 current STM scan of this structure. We observe the monolayer growing over step-edges of the un-  
74 derlying Cu(111) substrate. Weak interlayer interaction allows the van der Waals layer to have vary-  
75 ing relative rotational orientations,  $\theta \approx 0^\circ - 4^\circ$ , on the substrate corresponding to a Moiré pattern

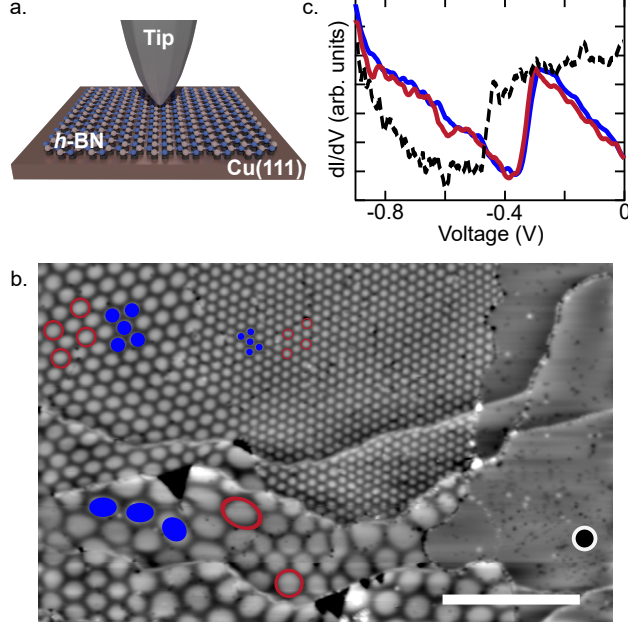


**Figure 1:** (a.) Scheme of the experiment. (b.) Large scale ( $200 \times 125 \text{ nm}^2$ ) constant-current ( $I = 20 \text{ pA}$ ,  $V = 3.7 \text{ V}$ ) STM topography of the  $h\text{-BN}/\text{Cu}(111)$  and bare  $\text{Cu}(111)$  surface. Blue circles and red rings mark exemplary valley and rim areas, respectively. (c.) Differential conductance  $dI/dV$  spectra taken at rim (red line) and valley (blue line) sites and at the bare  $\text{Cu}(111)$  substrate (dashed black line).

76 wavelength of  $\lambda \approx 3 \text{ nm} - 14 \text{ nm}$ . Furthermore, we observe a shift of the surface state onset of  
 77 the  $\text{Cu}(111)$  from  $\approx -480 \text{ meV}$  on the bare substrate to  $\approx -320 \text{ meV}$  on the  $h\text{-BN}/\text{Cu}(111)$  (Fig-  
 78 ure 1(c)) [32]. We found this shift to vary only marginally ( $\approx \pm 10 \text{ meV}$ ) with the Moiré periodicity  
 79 or between rim and valley sites [33,34].

80  $h\text{-BN}/\text{Cu}(111)$  is known to have an indirect bandgap of  $6.1 \text{ eV}$  [35] which can be modulated by the  
 81 Moiré pattern [30]. We analyse the substrate using STM topography,  $dI/dV$ , and frequency shift  
 82  $\Delta f$  AFM maps at low (in-gap) and high (conduction band onset) bias conditions (see Figure 2).  
 83 Due to  $h\text{-BN}$  being insulating, no spectroscopic contribution is expected at low bias voltages mak-  
 84 ing it transparent to STM, as seen in Figure 2(b, d). At this bias only Friedel oscillations due to the  
 85 scattering of the  $\text{Cu}(111)$  surface state electrons on defects and adsorbates are observed. Contrar-  
 86 ily, as Figure 2(a) reveals, at higher bias the STM topography corresponds to the modulation of the  
 87  $h\text{-BN}/\text{Cu}(111)$  interface state as we will show below.

88 Despite the large change in electronic density of states and thus tip height between the data ob-

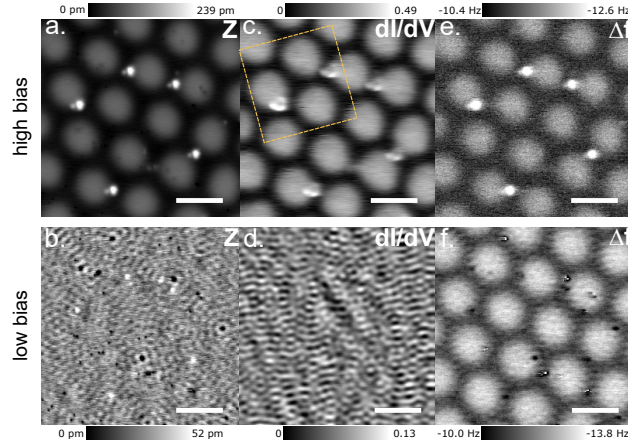


**Figure 2:** STM/AFM characterisation of *h*-BN/Cu(111) Moiré superstructure. (a., b.) Constant-current topography at  $I = 500$  pA and  $V = 3.6$  V (top) or  $V = 5$  mV (bottom). (c., d.) Simultaneously measured differential conductance ( $dI/dV$ ) maps ( $V_{\text{mod}} = 10$  mV (top) and  $V_{\text{mod}} = 1$  mV (bottom), respectively), and (e., f.) frequency shift ( $\Delta f$ ) maps ( $A_{\text{osc}} = 50$  pm). The dashed yellow box marks the area used for the  $\Phi$  maps. Scale bar: 10 nm.

99 tained at the two different sample biases, we observe a one to one correspondence between the si-  
 90 multaneously recorded  $\Delta f$  images and the STM topography. Also, the  $\Delta f$  variation between rim  
 91 and valley areas in both images changes only marginally. The additionally imaged adsorbates (dot  
 92 or ring like features) allow thereby the precise alignment between the subsequently acquired data  
 93 sets.

## 94 Work-function variation

95 While the work-function is generally discussed in the framework of a macroscopic quantity [36],  
 96 we will use the notation, valid also on the nanoscale, that  $\Phi$  is the local surface potential measured  
 97 from the Fermi level,  $E_F$  [37]. For a nano-patterned surface, such as *h*-BN/Cu(111),  $\Phi$  fluctuations  
 98 can originate from locally varying charge transfer between the substrate and the dielectric layer  
 99 [38-40].

100 In our studied substrate, it is the lattice mismatch between the *h*-BN and the Cu(111) substrate,  
 101 which leads to a varying atomic registry and subsequently induces a lateral modulation of the  
 102 charge transfer [41]. Additionally, this leads to in-plane electric fields which have been shown to  
 103 trap atoms, molecules, and nanoclusters [11,13,42].

104 To map the local  $\Phi$  fluctuations and to correlate them with the structural properties of the surface,  
 105 we use two complementary methods: the first method is based on the shift of the FER induced by  
 106  $\Phi$  variations. The effective potential well of depth  $\Phi$  at the surface of a metal can accommodate a  
 107 series of Rydberg states, extending a few  $\text{\AA}$  into the vacuum above the metal surface [43]. These  
 108 image potential states (IPSs) are delocalised in the surface plane and contain the full band of the  
 109 2D electron gas. However, the electric field exerted by the proximity of the probing tip distorts the  
 110 energy spacing of the IPSs and are referred as FER which are revealed in  $dI/dV$  measurements as  
 111 strong peaks at positive bias [43]. Figure 3(a) shows such spectra in which we observe a series of  
 112 peaks whose energies are strongly influenced by the measurement position. The non-trivial double  
 113 peak structure at approximately 3.5 – 4.5 V is due to varying contributions from the two interfaces  
 114 of the dielectric layer. We therefore evaluate the unambiguous shift of the 2nd peak at around 5.6 –  
 115 6.0 V as a measure for the local  $\Phi$  variation.

116 Our nc-AFM allows us to employ with KPFM a second, independent method to detect the variation  
 117 in  $\Phi$ . For this we record the frequency shift,  $\Delta f$ , of the resonance frequency of the perpendicu-  
 118 lar to the surface oscillating cantilever versus bias voltage (see Figure 3(b)). At the extrema of the  
 119 parabolic  $\Delta f$  curves, the electrostatic force is minimised by the applied voltage which compensates  
 120 the contact potential difference between  $\Phi$  of tip and  $\Phi$  of sample [44].

121 Using the shift of the FER we find an average variation between valley and rim regions of  $\Delta\Phi =$   
 122  $148 \pm 17$  meV which agrees well with previous observations [27,45]. Interestingly, however, we  
 123 find a significantly smaller average difference between valley and rim regions of only  $\Delta\Phi = 86 \pm$   
 124  $16$  meV when analysing the CPD data. This hints toward a lower lateral resolution of the KPFM  
 125 measurement compared to the FER map. The  $\Delta f$  signal in KPFM originates from the relatively  
 126 long-range electrostatic interaction which is therefore a weighted average over the relevant size of  
 127 tip (radii  $\approx 5 - 10$  nm [46]) that is of same order as the size of the rim and valley regions and, as  
 128 a result, lead to an underestimation of the  $\Delta\Phi$ . Nevertheless, both measurement techniques agree  
 129 well in their qualitative results as it is evident from the  $\Delta\Phi$  maps (see Figure 3(b,c)).

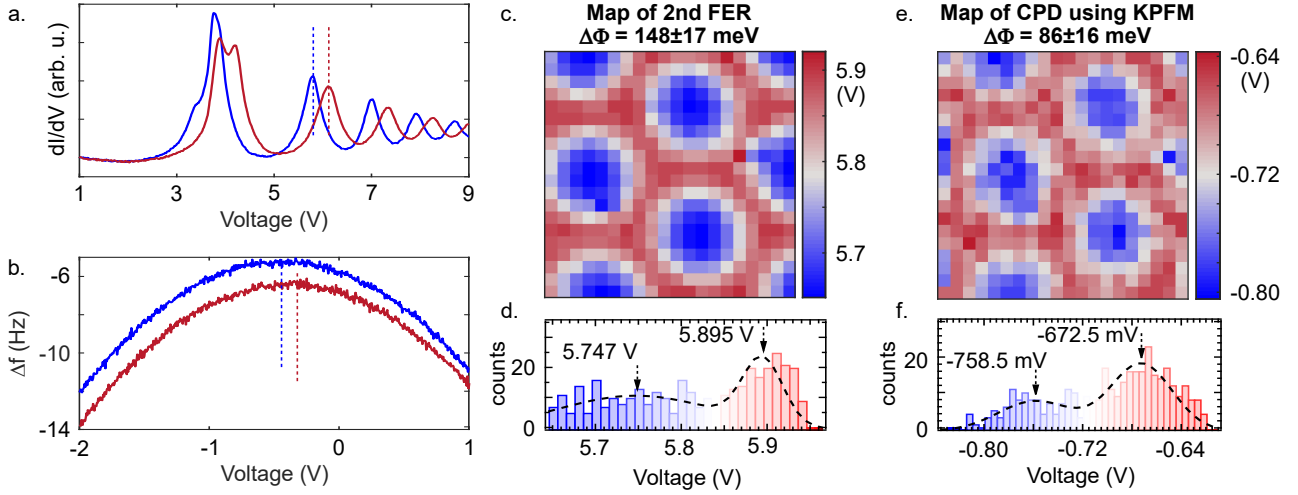


**Figure 3:** Work-function variation between rim (red) and valley (blue) areas measured using (a.)  $dI/dV$  at constant current ( $I = 100$  pA) and (b.) KPFM at constant height (stabilised in the valley at  $I = 100$  pA,  $V = 10$  mV,  $A_{\text{mod}} = 50$  pm), respectively. The dotted vertical lines mark exemplary FER and CPD values used for the spatially resolved plots shown in (c.) and (d.). The maps are taken at the yellow box indicated in Figure 2c on a  $20 \times 20$  grid over  $20 \times 20$  nm<sup>2</sup>. They display the position of the maximum of the second peak in the FER (c.) and the maximum of the KPFM parabola (e.), respectively. (d., f.) Histograms and fits for rim and valley where arrows mark the centre positions of the Gaussians used for the determination of the distribution centre.

### 130 Stiffness

131 Probing the force perpendicular to the substrate,  $F_{\perp}$ , at varying tip-sample separations  $z$ , the ef-  
 132 fective stiffness of a nanostructure can be evaluated by comparing the  $F_{\perp}(z)$  behaviour at different  
 133 areas of the Moiré superstructure [23]. Additionally, such set of data enables us to obtain maps of  
 134 constant tip-sample interaction forces that allow quantification of the corrugation of Moiré super-  
 135 structure.

136 To achieve such data we map the  $\Delta f$  signal at constant oscillation amplitude for an  $8 \times 8$  nm<sup>2</sup> area  
 137 at 28 relative tip-surface distances between  $z = 0$  and 270 pm. We define  $z = 0$  as the tip-sample  
 138 separation in the valley at  $I = 100$  pA and  $V = 10$  mV.

139 Using the matrix inversion method [47] we convert the 3D stack of  $\Delta f$  data into the out-of surface  
 140 force component  $F_{\perp}$ . The now obtained 3D force stack enables us to evaluate the interaction be-  
 141 tween the tip and the monolayer substrate without being strongly influenced by the electronic cor-  
 142 rugation as in STM only measurements. By taking a 2D cut at constant force through the 3D stack,



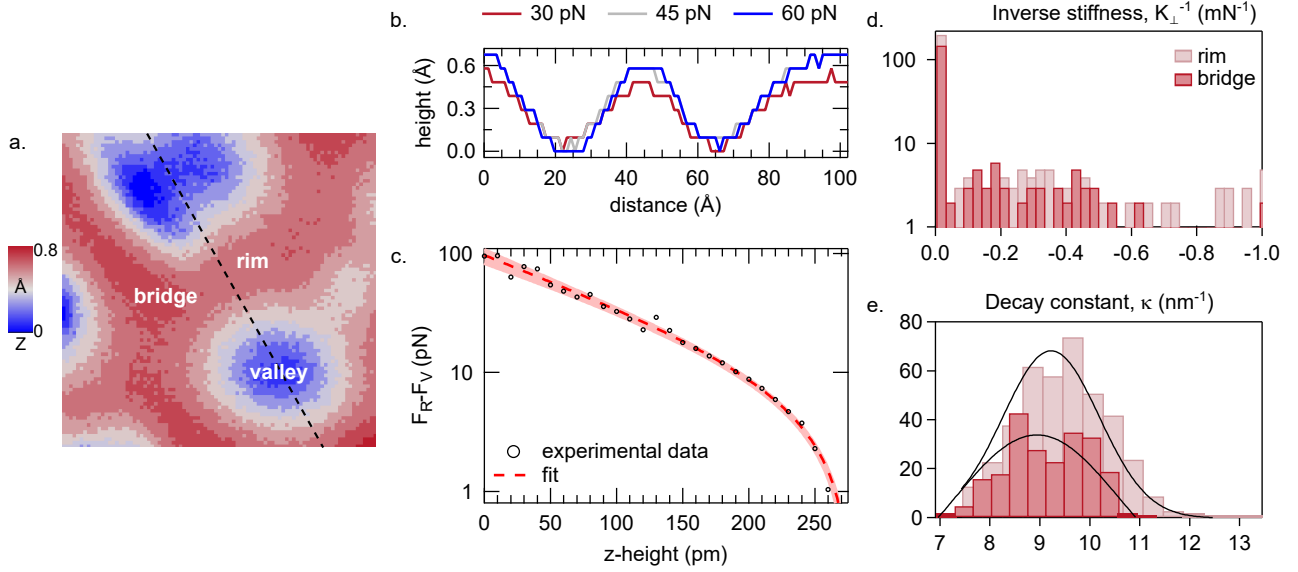


**Figure 4:** Local stiffness of  $h\text{-BN/Cu(111)}$ . (a.) Topography of a  $8 \times 8 \text{ nm}^2$   $h\text{-BN/Cu(111)}$  corresponding to a constant force  $F_{\perp} = 30 \text{ pN}$ . (b.) Line profiles taken from constant vertical force maps along the black dashed line in (a.), at  $F_{\perp} = 30 \text{ pN}$  (red),  $45 \text{ pN}$  (grey), and  $60 \text{ pN}$  (blue), respectively. (c.) Average short range force obtained for the rim and the bridge region after subtracting the contribution from valley area (dots) and fit (dashed line). The red area mark the 90% confidence range. (d.,e.) Histograms of inverse stiffness ( $K_{\perp}^{-1}$ ) and decay constant ( $\kappa$ ) of the rim (pink) and bridge sites (red), respectively.

143 we obtain a topography at a constant tip-substrate interaction force which allows us to visualise the  
 144 corrugation between rim and valley areas (see Figure 4(a)). Figure 4(b) shows different line profiles  
 145 corresponding to constant force values of  $F_{\perp} = 30 \text{ pN}$ ,  $45 \text{ pN}$ , and  $60 \text{ pN}$ . These line profiles reveal  
 146 an average corrugation of  $0.6 \pm 0.2 \text{ \AA}$  which agrees well with the corrugation of  $0.3 - 0.7 \text{ \AA}$  ob-  
 147 tained by Schwarz *et al.* [26]. In these line profiles we obtain a minimal corrugation increase at  
 148 increased constant force values which hints to some mechanical relaxations of the rim areas under  
 149 the influence of the force exerted by the tip.

150 To analyse this effect we separate the short-range forces which act between the tip apex and the  
 151 sample and which varies over the corrugation of the monolayer, from electrostatic and van der  
 152 Waals long-range forces by subtracting the average total force  $F_V$  measured in the valley areas (blue  
 153 regions in Fig. 4(a)) from the total forces  $F_R$  acting at rim and bridge sites of the superstructure  
 154 (red regions in Fig. 4(a)). The resulting difference  $F_D = F_R - F_V$  is the additional short-range

155 force which solely influences rim and bridge areas and which might locally lift the *h*-BN layer lead-  
 156 ing to an increase of corrugation. Figure 4(c) shows the over rim and bridge sites averaged  $F_D(z)$   
 157 which decays with  $z$  mainly exponentially as expected from an interatomic short-range force when  
 158 neglecting Pauli repulsion [23,48]. The over-exponential decay at  $z > 200$  pm is caused by a small  
 159 offset of  $F_0 \approx 1$  pN due to the finite set of  $\Delta f$  data which results in  $F_R \equiv F_V$  at the last measure-  
 160 ment height ( $z = 270$  pm, see Methods). A very soft *h*-BN-layer would show an additional over-  
 161 exponential increase at small  $z$  due to the lifting of the sheet by  $\Delta z = F_D(z)K_{\perp}^{-1}$ , where  $K_{\perp}$  is the  
 162 local vertical stiffness [23]. Assuming an exponential decay of the intrinsic short-range force be-  
 163 tween tip an substrate and compensating for any lifting, we get for the local vertical force,  $F_D$ , as a  
 164 function of relative height:

$$165 \quad F_D(z) = (\kappa/K_{\perp}) \times W_0(F_0\kappa/K_{\perp} \exp[-\kappa z]) + F_0, \quad (1)$$

166 where  $W_0$  is the real-valued branch of the Lambert  $W$  function and  $\kappa$  is the decay constant [23].  
 167 As shown in Figure 4(c) we obtain a good agreement between our data and the model. The best  
 168 fit yields a local vertical stiffness of  $K_{\perp} = 9.4 \pm 0.9$  N m<sup>-1</sup> (Figure 4(c)), which demonstrate the  
 169 high stiffness (negligible softness) of the *h*-BN monolayer on Cu(111) that is an order of magni-  
 170 tude higher than found on Rh(111) [23]. The statistical evaluation of the spatial variation of  $K_{\perp}$   
 171 is shown in Figure 4d. The dramatic peak at small inverse stiffness in both rim and bridge areas  
 172 means an almost perfect exponential behaviour of the short-range force and that *h* – BN/Cu(111)  
 173 undergoes no significant deformation. Also the histogram of the decay constant  $\kappa$  in Figure 4(e)  
 174 reveal only negligible differences between rim ( $\kappa = 9.2 \pm 1.3$  nm<sup>-1</sup>) and bridge areas ( $\kappa =$   
 175  $8.9 \pm 1.4$  nm<sup>-1</sup>) indicating almost no difference in the mechanical properties between different  
 176 areas of the Moiré superstructure.

## 177 **Conclusion**

178 In summary, we report the electronic and mechanical characterisation of *h*-BN/Cu(111) using an  
179 STM/AFM. Our STM studies corroborate that the *h*-BN monolayer is only weakly coupled to  
180 the Cu(111) surface as is evidenced by the large angular range of Moiré superstructures observed  
181 which in turn leads to work-function patterning. Using FER and KPFM maps we report a work-  
182 function variation of  $148 \pm 17$  and  $86 \pm 16$  meV, respectively, which agrees well with the previous  
183 experimental and theoretical studies [27,45].

184 3D force maps, obtained by constant height  $\Delta f$  imaging, allow us to test the mechanical stability of  
185 the monolayer substrate in the short-range force regime. Using the AFM tip as a nanoindenter we  
186 probe its effect on the *h*-BN/Cu(111) system. We obtain a sheet stiffness of  $K_{\perp} = 9.4 \pm 0.9$  N m<sup>-1</sup>,  
187 which is an order of magnitude larger than that obtained on *h*-BN/Rh(111), indicating substantial  
188 mechanical stability. Small lattice mismatch between *h*-BN and Cu(111) as compared to *h*-BN and  
189 Rh(111) results in lower strain and no buckling of the substrate leading to high stiffness. Further-  
190 more, our results corroborate that *h*-BN/Cu(111) has a small corrugation of  $0.6 \pm 0.2$  Å but is  
191 mechanically stiff making it an appealing platform for studying intrinsic electronic and mechanical  
192 properties of nanostructures.

## 193 **Experimental**

194 We employ a custom-built ultra-high vacuum ( $< 10^{-10}$  mbar) low-temperature ( $T = 1.4$  K)  
195 nc-AFM operated in frequency-modulated mode. A stiff qPlus cantilever design [49] ( $k_0 =$   
196  $1800$  N m<sup>-1</sup>,  $f_0 = 29077$  Hz,  $Q = 60000$ ) at an oscillation amplitude  $A = 50$  pm enables the nc-  
197 AFM functionality [50]. The bias voltage  $V$  is applied to the substrate and the tunnelling current  $I$   
198 is measured at the virtually grounded tip. The STM/AFM images were processed with the Gwyd-  
199 dion software [51].

200 **FER and KPFM measurements:** FER measurements are taken by modulating  $V$  ( $f_m = 607$  Hz,  
201  $V_m = 10$  mV peak-to-peak) and detecting the  $dI/dV$  signal with lock-in technique while the tip  
202 height is adjusted so that the current  $I$  remains constant (constant current mode) during the bias

203 sweep. For KPFM measurements we stabilise the tip height at  $I = 100$  pA and  $V = 10$  mV. We  
204 then record the frequency shift  $\Delta f$  with respect to  $f_0$  while  $V$  is swept at constant tip height.  
205 **Vertical stiffness:** The 3D  $\Delta f$  data ( $8 \times 8 \times 0.27$  nm<sup>3</sup>), evaluated in this work, are obtained by  
206 taking 28 2D maps at successively increased tip-sample separation ( $\Delta z = 10$  pm) starting from a tip  
207 height stabilised at  $I = 100$  pA,  $V = 10$  mV. We use the exponential dependence of average current  
208 as the tip is retracted to compensate for  $z$ -drift over  $\approx 23$  h of data acquisition time.  
209 **Sample preparation:** A Cu(111) single crystal (MaTeck GmbH) is cleaned via repeated cycles of  
210 Ar-ion sputtering at room temperature followed by annealing to 1020 K in an ultra-high vacuum  
211 preparation chamber. A partial layer of  $h$ -BN is grown by chemical vapour deposition (CVD) by  
212 heating the Cu(111) sample to 980 K and exposing it to 25 L of borazine ((HBNH)<sub>3</sub>) gas (Katchem  
213 spol s.r.o.).  $h$ -BN grows in a self-terminating growth process [52]. It is then transferred in-situ to  
214 the nc-AFM for characterisation.

## 215 Acknowledgements

216 A. G., M. M., and M. T. acknowledge support from the Collaborative Research Center (SFB) 767  
217 of the German Research Foundation (DFG) for financial support. M. T. acknowledges support by  
218 the Heisenberg Program (Grant No. TE 833/2-1) and the Priority Programme (SPP) 2244 of the  
219 DFG and Y. W. would like to thank support from Alexander von Humboldt Foundation through  
220 a Humboldt Research Fellowship for Postdoctoral Researchers. We would also like to thank W.  
221 Auwärter for stimulating discussions.

## 222 References

- 223 1. Novoselov, K. S.; Geim, A. K.; Morozov, S. V.; Jiang, D.; Zhang, Y.; Dubonos, S. V.; Grig-  
224 orieva, I. V.; Firsov, A. A. *Science* **2004**, *306* (5696), 666–669. doi:10/bcqksc.
- 225 2. Novoselov, K. S.; Mishchenko, A.; Carvalho, A.; Castro Neto, A. H. *Science* **2016**, *353*  
226 (6298), . doi:10/f8w86m.

- 227 3. Watanabe, K.; Taniguchi, T.; Kanda, H. *Nature Materials* **2004**, *3* (6), 404–409. doi:10.1038/  
228 nmat1134.
- 229 4. Dean, C. R.; Young, A. F.; Meric, I.; Lee, C.; Wang, L.; Sorgenfrei, S.; Watanabe, K.;  
230 Taniguchi, T.; Kim, P.; Shepard, K. L.; Hone, J. *Nature Nanotechnology* **2010**, *5* (10),  
231 722–726. doi:10/fjfcht.
- 232 5. Xue, J.; Sanchez-Yamagishi, J.; Bulmash, D.; Jacquod, P.; Deshpande, A.; Watanabe, K.;  
233 Taniguchi, T.; Jarillo-Herrero, P.; LeRoy, B. J. *Nature Materials* **2011**, *10* (4), 282–285.  
234 doi:10/d4k5vp.
- 235 6. Britnell, L.; Gorbachev, R. V.; Jalil, R.; Belle, B. D.; Schedin, F.; Mishchenko, A.; Geor-  
236 giou, T.; Katsnelson, M. I.; Eaves, L.; Morozov, S. V.; Peres, N. M. R.; Leist, J.; Geim, A. K.;  
237 Novoselov, K. S.; Ponomarenko, L. A. *Science* **2012**, *335* (6071), 947–950. doi:10/hqc.
- 238 7. Pakdel, A.; Bando, Y.; Golberg, D. *Chemical Society Reviews* **2014**, *43* (3), 934–959. doi:10/  
239 gf6bpz.
- 240 8. Li, Q.; Zou, X.; Liu, M.; Sun, J.; Gao, Y.; Qi, Y.; Zhou, X.; Yakobson, B. I.; Zhang, Y.; Liu, Z.  
241 *Nano Letters* **2015**, *15* (9), 5804–5810. doi:10/f7rnhm.
- 242 9. Cui, X.; Lee, G.-H.; Kim, Y. D.; Arefe, G.; Huang, P. Y.; Lee, C.-H.; Chenet, D. A.;  
243 Zhang, X.; Wang, L.; Ye, F.; Pizzocchero, F.; Jessen, B. S.; Watanabe, K.; Taniguchi, T.;  
244 Muller, D. A.; Low, T.; Kim, P.; Hone, J. *Nature Nanotechnology* **2015**, *10* (6), 534–540.  
245 doi:10/gf3chz.
- 246 10. Mendelson, N.; Xu, Z.-Q.; Tran, T. T.; Kianinia, M.; Scott, J.; Bradac, C.; Aharonovich, I.;  
247 Toth, M. *ACS Nano* **2019**, *13* (3), 3132–3140. doi:10/gfx5zq.
- 248 11. Bose, S.; García-García, A. M.; Ugeda, M. M.; Urbina, J. D.; Michaelis, C. H.; Brihuega, I.;  
249 Kern, K. *Nature Materials* **2010**, *9* (7), 550–554. doi:10/b49wjp.

- 250 12. Kahle, S.; Deng, Z.; Malinowski, N.; Tonnoir, C.; Forment-Aliaga, A.; Thontasen, N.;  
251 Rinke, G.; Le, D.; Turkowski, V.; Rahman, T. S.; Rauschenbach, S.; Ternes, M.; Kern, K.  
252 *Nano Letters* **2012**, *12* (1), 518–521. doi:10/cqn9hd.
- 253 13. Joshi, S.; Bischoff, F.; Koitz, R.; Ecija, D.; Seufert, K.; Seitsonen, A. P.; Hutter, J.; Diller, K.;  
254 Urgel, J. I.; Sachdev, H.; Barth, J. V.; Auwärter, W. *ACS Nano* **2014**, *8* (1), 430–442. doi:10/  
255 gf3chd.
- 256 14. Jacobson, P.; Herden, T.; Muenks, M.; Laskin, G.; Brovko, O.; Stepanyuk, V.; Ternes, M.;  
257 Kern, K. *Nature Communications* **2015**, *6*, 8536. doi:10/f7zbpd.
- 258 15. Muenks, M.; Jacobson, P.; Ternes, M.; Kern, K. *Nature Communications* **2017**, *8* (1), 14119.  
259 doi:10.1038/ncomms14119.
- 260 16. Will, M.; Atodiresei, N.; Caciuc, V.; Valerius, P.; Herbig, C.; Michely, T. *ACS Nano* **2018**, *12*  
261 (7), 6871–6880. doi:10/gd3jgf.
- 262 17. Mehler, A.; Néel, N.; Kröger, J. *The Journal of Physical Chemistry Letters* **2020**, *11* (13),  
263 5204–5211. doi:10.1021/acs.jpcllett.0c01320.
- 264 18. Riss, A.; Richter, M.; Paz, A. P.; Wang, X.-Y.; Raju, R.; He, Y.; Ducke, J.; Corral, E.; Wut-  
265 tke, M.; Seufert, K.; Garnica, M.; Rubio, A.; V. Barth, J.; Narita, A.; Müllen, K.; Berger, R.;  
266 Feng, X.; Palma, C.-A.; Auwärter, W. *Nature Communications* **2020**, *11* (1), 1490. doi:  
267 10.1038/s41467-020-15210-2.
- 268 19. Nagashima, A.; Tejima, N.; Gamou, Y.; Kawai, T.; Oshima, C. *Physical Review Letters* **1995**,  
269 *75* (21), 3918–3921. doi:10.1103/PhysRevLett.75.3918.
- 270 20. Auwärter, W.; Kreutz, T. J.; Greber, T.; Osterwalder, J. *Surface Science* **1999**, *429* (1),  
271 229–236. doi:10/cnztjm.
- 272 21. Corso, M.; Auwärter, W.; Muntwiler, M.; Tamai, A.; Greber, T.; Osterwalder, J. *Science* **2004**,  
273 *303* (5655), 217–220. doi:10/bk86qd.

- 274 22. Berner, S.; Corso, M.; Widmer, R.; Groening, O.; Laskowski, R.; Blaha, P.; Schwarz, K.; Go-  
275 riachko, A.; Over, H.; Gsell, S.; Schreck, M.; Sachdev, H.; Greber, T.; Osterwalder, J. *Ange-  
276 wandte Chemie International Edition* **2007**, *46* (27), 5115–5119. doi:10/c5fjgc.
- 277 23. Herden, T.; Ternes, M.; Kern, K. *Nano Letters* **2014**, *14* (6), 3623–3627. doi:10/f56gqk.
- 278 24. Schulz, F.; Drost, R.; Hämäläinen, S. K.; Demonchaux, T.; Seitsonen, A. P.; Liljeroth, P. *Phys-  
279 ical Review B* **2014**, *89* (23), 235429. doi:10/gf3chx.
- 280 25. Laskowski, R.; Blaha, P.; Schwarz, K. *Physical Review B* **2008**, *78* (4), 045409. doi:10/cg3cfg.
- 281 26. Schwarz, M.; Riss, A.; Garnica, M.; Ducke, J.; Deimel, P. S.; Duncan, D. A.; Thakur, P. K.;  
282 Lee, T.-L.; Seitsonen, A. P.; Barth, J. V.; Allegretti, F.; Auwärter, W. *ACS Nano* **2017**, *11* (9),  
283 9151–9161. doi:10/gbvhd5.
- 284 27. Joshi, S.; Ecija, D.; Koitz, R.; Iannuzzi, M.; Seitsonen, A. P.; Hutter, J.; Sachdev, H.; Vija-  
285 yaraghavan, S.; Bischoff, F.; Seufert, K.; Barth, J. V.; Auwärter, W. *Nano Letters* **2012**, *12*  
286 (11), 5821–5828. doi:10.1021/nl303170m.
- 287 28. Siegel, G.; Ciobanu, C. V.; Narayanan, B.; Snure, M.; Badescu, S. C. *Nano Letters* **2017**, *17*  
288 (4), 2404–2413. doi:10/f9vwn3.
- 289 29. Brülke, C.; Heepenstrick, T.; Humberg, N.; Krieger, I.; Sokolowski, M.; Weiß, S.; Tautz, F. S.;  
290 Soubatch, S. *The Journal of Physical Chemistry C* **2017**, *121* (43), 23964–23973. doi:10/  
291 gckcn6.
- 292 30. Zhang, Q.; Yu, J.; Ebert, P.; Zhang, C.; Pan, C.-R.; Chou, M.-Y.; Shih, C.-K.; Zeng, C.;  
293 Yuan, S. *ACS Nano* **2018**, *12* (9), 9355–9362. doi:10.1021/acsnano.8b04444.
- 294 31. Baykara, M. Z.; Schwarz, U. D. 3D Force Field Spectroscopy. In *Noncontact Atomic Force  
295 Microscopy: Volume 3*; Morita, S., Giessibl, F. J., Meyer, E., Wiesendanger, R., Eds.;  
296 NanoScience and Technology; Springer International Publishing: Cham, 2015; pp 9–28.  
297 doi:10.1007/978-3-319-15588-3\_2.

- 298 32. Crommie, M. F.; Lutz, C. P.; Eigler, D. M. *Nature* **1993**, *363* (6429), 524–527. doi:10.1038/  
299 363524a0.
- 300 33. De Renzi, V.; Rousseau, R.; Marchetto, D.; Biagi, R.; Scandolo, S.; del Pennino, U. *Physical*  
301 *Review Letters* **2005**, *95* (4), 046804. doi:10/ch4bc5.
- 302 34. Zioff, J.; Gold, P.; Bendounan, A.; Forster, F.; Reinert, F. *Surface Science* **2009**, *603* (2),  
303 354–358. doi:10/dcg2kf.
- 304 35. Cassabois, G.; Valvin, P.; Gil, B. *Nature Photonics* **2016**, *10* (4), 262–266. doi:10.1038/  
305 nphoton.2015.277.
- 306 36. Kittel, C.; McEuen, P.; Sons, J. W. . *Introduction to Solid State Physics*; John Wiley & Sons,  
307 Limited, 2018.
- 308 37. Wandelt, K. *Applied Surface Science* **1997**, *111*, 1–10. doi:10.1016/S0169-4332(96)00692-7.
- 309 38. Ploigt, H.-C.; Brun, C.; Pivetta, M.; Patthey, F.; Schneider, W.-D. *Physical Review B* **2007**, *76*  
310 (19), 195404. doi:10/fknqpt.
- 311 39. Ruffieux, P.; Ait-Mansour, K.; Bendounan, A.; Fasel, R.; Patthey, L.; Gröning, P.; Gröning, O.  
312 *Physical Review Letters* **2009**, *102* (8), 086807. doi:10/bhqpbw.
- 313 40. Borca, B.; Barja, S.; Garnica, M.; Sánchez-Portal, D.; Silkin, V. M.; Chulkov, E. V.; Her-  
314 manns, C. F.; Hinarejos, J. J.; Vázquez de Parga, A. L.; Arnau, A.; Echenique, P. M.; Mi-  
315 randa, R. *Physical Review Letters* **2010**, *105* (3), 036804. doi:10/fbf2xf.
- 316 41. Bokdam, M.; Brocks, G.; Katsnelson, M. I.; Kelly, P. J. *Physical Review B* **2014**, *90* (8),  
317 085415. doi:10/gf6bp2.
- 318 42. N’Diaye, A. T.; Bleikamp, S.; Feibelman, P. J.; Michely, T. *Physical Review Letters* **2006**, *97*  
319 (21), 215501. doi:10.1103/PhysRevLett.97.215501.



- 320 43. Gundlach, K. H. *Solid-State Electronics* **1966**, 9 (10), 949–957. doi:10.1016/0038-1101(66)  
321 90071-2.
- 322 44. Melitz, W.; Shen, J.; Kummel, A. C.; Lee, S. *Surface Science Reports* **2011**, 66 (1), 1–27.  
323 doi:10/dpzdck.
- 324 45. Gómez Díaz, J.; Ding, Y.; Koitz, R.; Seitsonen, A. P.; Iannuzzi, M.; Hutter, J. *Theoretical*  
325 *Chemistry Accounts* **2013**, 132 (4), 1350. doi:10.1007/s00214-013-1350-z.
- 326 46. Zerweck, U.; Loppacher, C.; Otto, T.; Grafström, S.; Eng, L. M. *Physical Review B* **2005**, 71  
327 (12), 125424. doi:10/b572bs.
- 328 47. Giessibl, F. J. *Applied Physics Letters* **2000**, 78 (1), 123–125. doi:10.1063/1.1335546.
- 329 48. Ternes, M.; Gonzalez, C.; Lutz, C. P.; Hapala, P.; Giessibl, F. J.; Jelinek, P.; Heinrich, A. J.  
330 *Phys. Rev. Lett.* **2011**, 106, 016802.
- 331 49. Giessibl, F. J.; Hembacher, S.; Herz, M.; Schiller, C.; Mannhart, J. *Nanotechnology* **2004**, 15  
332 (2), S79. doi:10/c4phmm.
- 333 50. Münks, M. Scanning Tunneling Microscopy and Atomic Force Microscopy Measurements on  
334 Correlated Systems. Ph. D. Thesis, Universität Konstanz: Konstanz, 2017.
- 335 51. Nečas, D.; Klapetek, P. *Open Physics* **2011**, 10 (1), 181–188. doi:10/bjn3cr.
- 336 52. Nagashima, A.; Tejima, N.; Gamou, Y.; Kawai, T.; Oshima, C. *Physical Review Letters* **1995**,  
337 75 (21), 3918–3921. doi:10.1103/PhysRevLett.75.3918.